REPORT DOCUMENTATION PAGE

Form Approved
OMB No. 0704-0188

Public reporting burden for this collection of information is estimated to average 1 hour per response, including the time for reviewing instructions, searching existing data sources, gathering and maintaining the data needed, and completing and reviewing the collection of information. Send comments regarding this burden estimate or any other aspect of this collection of information, including suggestions for reducing this burden, to Washington Headquarters Services, Directorate for Information Operations and Reports, 1215 Jefferson Davis Highway, Suite 1204, Arlington, CA 22202-4302, and to the Office of Management and Budget, Paperwork Reduction Project (0704-0188), Washington, DC 20503.

1. AGENCY USE ONLY (Leave blank)	2. REPORT DATE 00 Feb 28	3. REPORT TYPE AND DATES COVERED Final Report 6/01/99-2/28/00

4. TITLE AND SUBTITLE

INTEGRATED DETECTOR TECHNOLOGY FOR CORROSION INSPECTION

5. FUNDING NUMBERS

F49620-99-C-0032

6. AUTHOR(S)

Jerel A. Smith

7. PERFORMING ORGANIZATION NAME(S) AND ADDRESS(ES)

ARACOR
425 Lakeside Drive
Sunnyvale, CA 94086

8. PERFORMING ORGANIZATION REPORT NUMBER

P014FR-00

9. SPONSORING/MONITORING AGENCY NAME(S) AND ADDRESS(ES)

USAF, AFMC
Air Force Office of Scientific Research
801 N Randolph St, Suite 732
Arlington, VA 22203-1977

10. SPONSORING/MONITORING AGENCY REPORT NUMBER

11. SUPPLEMENTARY NOTES

12.a DISTRIBUTION/AVAILABILITY STATEMENT

Approved for public release; distribution is unlimited.

12.b DISTRIBUTION CODE

13. ABSTRACT *(Maximum 200 words)*

This project investigated the use of gas micro-strip detectors as a means of improving the throughput of an innovative technique for detecting hidden corrosion in aging aircraft. The evaluations included the development of system, detector and data-readout concepts capable of meeting the resolution and throughput goals for this instrument, and the modeling and computation of x-ray and electron interactions in the detector.

The results of this evaluation indicate that these detectors can be adapted to this application and can achieve the spatial resolution and count rates required to support a system throughput up to 25 m/hr for detection of 5% corrosion in lapjoints. This throughput, nearly two orders-of-magnitude faster than the existing demonstration system, is sufficient to support the use of this instrument as a practical adjunct to existing technologies. The next step in development would be the fabrication of this detector and the demonstration that the sensitivity and throughput targets can be achieved in a demonstration system.

14. SUBJECT TERMS

X-ray NDE, Corrosion Inspection, Aging Aircraft, Micro-Gap Detectors, Lap-joint corrosion, Rayleigh/Compton Ratio

15. NUMBER OF PAGES 21

16. PRICE CODE

17. SECURITY CLASSIFICATION OF REPORT	18. SECURITY CLASSIFICATION OF THIS PAGE	19. SECURITY CLASSIFICATION OF ABSTRACT	20. LIMITATION OF ABSTRACT
UNCLASSIFIED	UNCLASSIFIED	UNCLASSIFIED	UNLIMITED

NSN 7540-01-280-5500

Standard Form 298 (Rev.2-89)
Prescribed by ANSI Sta.239-18
298-102

INTEGRATED DETECTOR TECHNOLOGY FOR CORROSION INSPECTION

SUMMARY

This project investigated the use of gas micro-strip detectors as a means of improving the throughput of an innovative technique for detecting hidden corrosion in aging aircraft. The evaluations included the development of system, detector and data-readout concepts capable of meeting the resolution and throughput goals for this instrument, and the modeling and computation of x-ray and electron interactions in the detector.

The results of this evaluation indicate that these detectors can be adapted to this application and can achieve the spatial resolution and count rates required to support a system throughput up to 25 m/hr for detection of 5% corrosion in lapjoints. This throughput, nearly two orders-of-magnitude faster than the existing demonstration system, is sufficient to support the use of this instrument as a practical adjunct to existing technologies. The next step in development would be the fabrication of this detector and the demonstration that the sensitivity and throughput targets can be achieved in a demonstration system.

INTRODUCTION:

Corrosion is the number one maintenance problem confronting the US Air Force. Corrosion in lap-joints is a problem of sufficient magnitude to justify the development of an NDE instrument, if a reasonably priced, high-throughput, detector is available. This research has been directed toward developing and evaluating the technology required to design and fabricate such a detector.

ARACOR's instrumental concept, called COREX, is based on the energy-discriminated detection of x rays backscattered from the region of suspected corrosion. This research program has built upon a previous Air Force PRDA in which ARACOR developed the instrumental concept and upon an ongoing program through the UDRI to demonstrate its effectiveness at detecting corrosion in aircraft lap-joints.

While the previous programs have demonstrated that the detective modality is effective in manifesting low-levels of corrosion products in aircraft lap-joints, the demonstration technology, which uses discrete Xenon proportional counters and NIM electronics is too slow and expensive to be practical for use as an inspection tool. In response, ARACOR has developed a concept

using integrated proportional-counter array technologies developed for high-energy particle accelerators.

PROGRAM OBJECTIVES

Our goal, for this effort, has been to evaluate critical issues which could lead to an early evaluation of the practicability of the integrated-detector concept and which would develop tools and models to set the strategic outline of the subsequent technology development.

The specific objectives were:

1) **Develop a model of the x-ray and initial photoelectron interactions in the detector:**

   For a micro-Gap detector geometry used with high-pressure Xenon gas, model absorption of the incident x-ray spectrum, escape of the Xe-K fluorescence, and primary photo-electron emission from the substrate. Determine the pulse-height spectrum and the measurement throughput.

2) **Develop a model of the electron avalanche and ion transport in the detector:**

   For a given geometry (*i.e.* size and spacing of the electrode structures) and gas pressure, calculate the gain and temporal response of a unit cell of the detector.

TECHNICAL RESULTS

Since the original proposal for this research was written, the technological context of this work has continued to evolve. In particular, one technology, eddy current, has emerged as the Air Force's primary instrument for detection of lap-joint corrosion in aging aircraft. This does not obviate the need for the COREX technology; the "false-positive" indication rate of the eddy-current instruments is high enough that there is a pressing need to verify the presence of corrosion before expensive repairs are undertaken. However, as a secondary instrument, the emphasis for the COREX instrument will be more on keeping production costs low than on achieving high inspection throughput. While this has colored our thinking about what this instrument will look like, the major cost/throughput tradeoff decisions will take place in the development of the prototype; the proposed use of an integrated detector technology still appears to be the best way to minimize fabrication costs.

The detector technologies discussed in the proposal, the micro-strip gas chamber (MSGC), the micro-gap chamber (MGC), and the various mesh-based techniques have continued their

2

development and evaluation.[1-12] Of these, the MGC appears to be best for our application due to its greater fabrication simplicity, freedom from charging effects and physical robustness. We have used this technology as our baseline, however, we are spectators in the rapid development of these technologies. Any of these could most likely be adapted for use with our concept with some modification to our design and some customization of the technology "as developed."
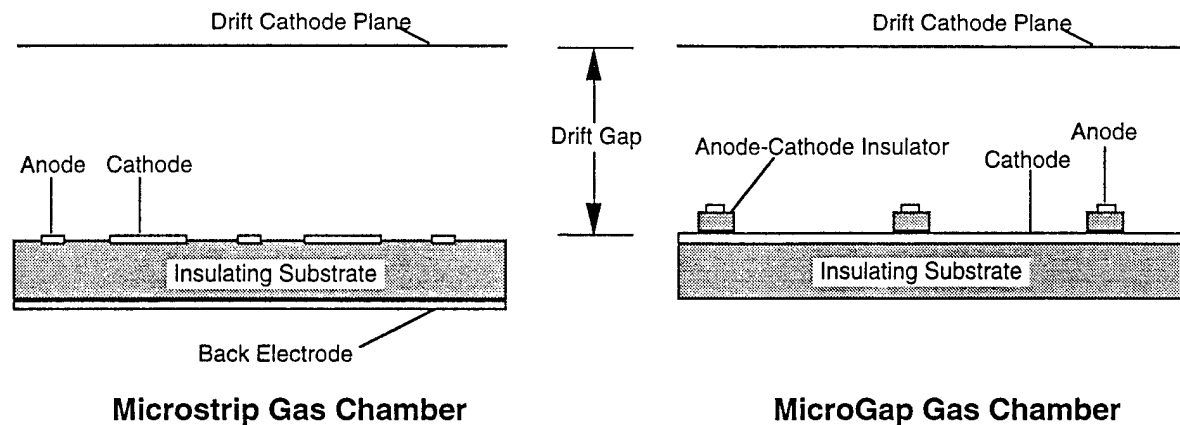

Figure 1. *The elements of the MSGC and MGC are shown here (not to scale). The space between the electrode structure and the Drift Cathode Plane is filled with an absorbing counter gas (typically Ne, Ar, or Xe mixed with a quench gas). Typical spacing (Anode to Anode) is 200 µm, while the drift gap is typically 3-10 mm.*

The electrode structures of the MSGC and MGC are illustrated in Figure 1. In both detectors, the proportional-counter avalanche occurs in the small (A-K) gap between the anode and cathode. Because minimal ion current flows back to the drift cathode, most of the current is captured very quickly. One problem with the MSGC has been the charging of the substrate in the A-K gap. The design of the MGC largely obviates this problem.

The strategic approach for this program began by laying out an optimal system geometry and a definition of the x-ray and detector optics. We then built an x-ray model to evaluate the performance. The desired performance characteristics, and the detector geometry raised a number of feasibility questions, particularly the feasibility of simultaneously meeting the energy and spatial resolution without giving up the open geometry and count rate. In addressing the feasibility questions, alternatives and modifications were introduced until we achieved an optimized solution.

SYSTEM AND DETECTOR CONFIGURATIONS

The final configuration of the system is shown to scale in Figure 2. A number of issues for the detector design—collimation angles, drift distances, spatial resolution, gas-pressure, x-ray capture and escape—needed to be evaluated in a specific geometrical context to be meaningful. The x-ray source is based on that which has been used in the previous research. To maximize the throughput, a compact geometry was used and the acceptance angles of the detector were opened up a much as possible within constraints posed by the requirements for spatial and angular resolution. It is expected that a second detector package will be located to the left side of the source. It was left out of the figure for graphical clarity.
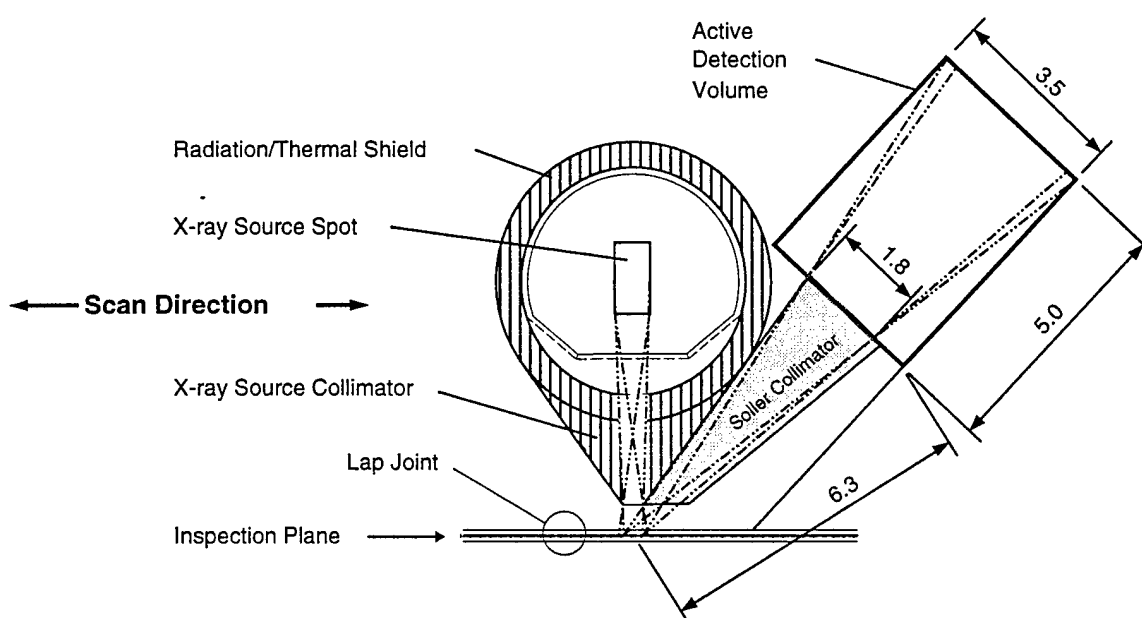

Figure 2. *This cross-section of the system shows the spatial relationships between the components and the optical constraints of the collimators. The system scans a swath along the lap-joint parallel to the plane of this view. The x rays are collimated in a fan which spreads across the lap joint; the illuminated surface is a 4-mm wide strip which runs normal to the page. X rays scattered from the lap-joint volume are collimated into planes parallel to the page. The dashed lines show the umbral and penumbral extents of the collimated beams.*

The performance goals for the system, and, by derivation, the detector, are based on experience with a two-channel breadboard system which has been fabricated and tested at ARACOR. The performance objectives for the new system are:

Detection Standard: The system is evaluated in terms of its ability to detect the oxidation of 5% of the aluminum in a lap-joint made from two 1-mm thick sheets.

4

Spatial Resolution: The existing breadboard system views a volume element approximately 4-mm in diameter. The images sample the inspection region on a 2-mm grid; this appears to be about optimal. The goal was for the new system to match these values.

Throughput: Using two detectors, the breadboard system takes approximately 1/2 second to obtain a single data point with a signal-to-noise ratio (SNR) of 1:1 for the detection standard. During the evaluations referred to above, we found that, at an SNR of 1:1, patterns of corrosion could be confidently identified. The goal was to increase the throughput by 1–2 orders of magnitude.

The detector concept is illustrated in Figure 3. The parameters in this concept, (materials, potentials, and dimensions) have been chosen to meet the performance goals of the system.
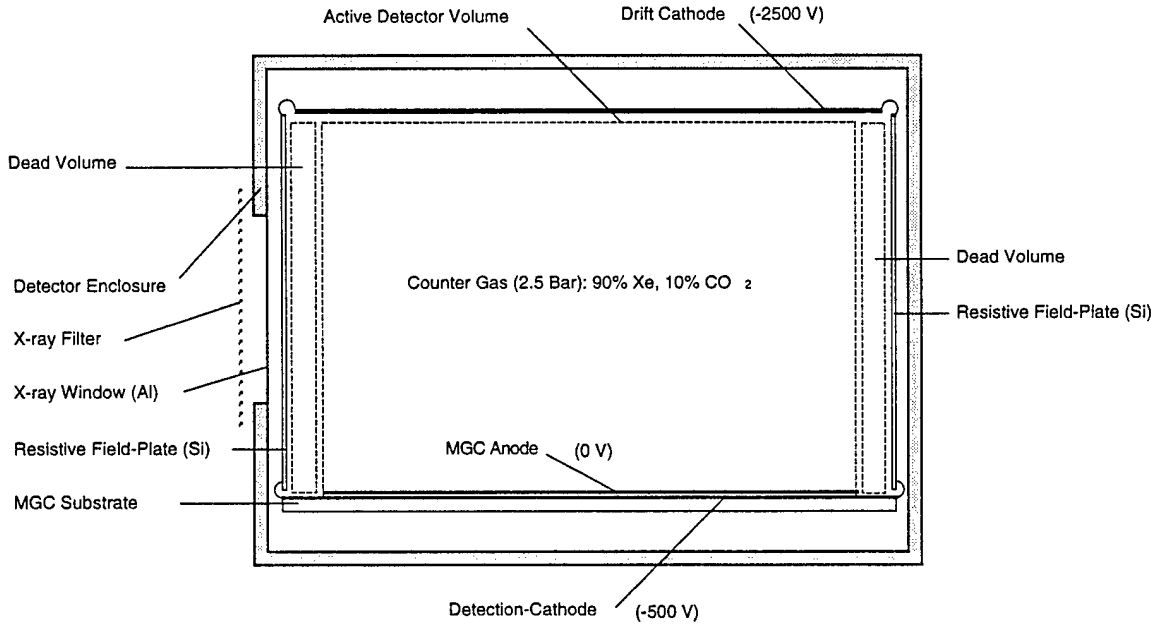

Figure 3. *The detector concept is shown from the same direction used in Figure 2. In this design, no radiation impinges on the cathode or MGC surfaces—greatly reducing photoemission problems. The resistive field plates keep the electric potential surfaces in a plane-parallel geometry. The active volume is similarly constrained by resistive field plates along the surfaces parallel to the page.*

THE X-RAY PERFORMANCE MODEL

The signal received in the detector, for x rays of coherently-scattered from aluminum in the volume element (voxel) being inspected, can be written,

$$I_{Al,coh} = I_0 e^{-\mu_{in}\rho t / Cos(\theta_{in})} \frac{m_{vox}}{D_s^2} \frac{\partial \sigma_{Al,coh}(\theta_{scat})}{\partial \Omega} e^{-\mu_{out}\rho t / Cos(\theta_{out})} \Omega_{det} \varepsilon_{det}$$

(1)

5

where explicit energy dependence has not been shown. The terms in this equation are:

E_{in}	keV	The energy of the x ray as it leaves the source and is incident on the sample,
E_{out}	keV	The energy of the x ray as it leaves the sample and is incident at the detector,
$I_{Al,coh}(E_{in})$	x ray/keV-sr-s	Detected signal,
I_0	x ray/keV-sr-s	X-ray source spectrum,
$\mu_{in}(E_{in})$	cm^2/g	Absorption coefficient for x rays entering the volume element and being attenuated by the overlying sheet of aluminum,
$\mu_{out}(E_{out})$	cm^2/g	Absorption coefficient for x rays leaving the volume element and being attenuated by the overlying sheet of aluminum,
ρt	g/cm^2	Product of density and thickness for the overlaying layer,
θ_{in}	rad	Angle of entrance to the voxel (0 for this model),
θ_{out}	rad	Angle of exit from the voxel ($3\pi/4$ for this model),
θ_{scat}	rad	Scattering angle ($3\pi/4$ for this model),
m_{vox}	g	Mass of aluminum in the voxel,
D_s	cm	Distance from the source spot to the voxel,
$\dfrac{\partial \sigma_{Al,coh}(Ein, \theta_{scat})}{\partial \Omega}$	cm^2/g-sr	Partial differential scattering cross-section for coherent scatter from aluminum,
Ω_{det}	sr	Solid angle of the detector as seen from the voxel, and
$\varepsilon_{det}(E_{out})$		Quantum efficiency of the detector.

Angular variations in the scatter of the x rays must be tracked accurately; the scattering distributions in this energy range show very strong angular dependence, with the coherent (also called Rayleigh) scatter being strongly peaked in the forward direction. The signal detected for incoherent (also called Compton) scatter and for scatter from oxygen can be similarly written with a change in the choice in partial differential cross section. For coherent scatter, the x-ray energy is unchanged by the scattering process. However, there is an energy loss in incoherent scattering,

$$E_{out} = \frac{E_{in}}{1 + (E_{in}/m_e c^2)(1 - Cos(\theta_{scat}))} \qquad (2)$$

where $m_e c^2$ is the rest mass of the electron in keV.

The x rays interact in the detector either through coherent scatter, Compton scatter or photoelectric absorption. The coherent scatter is elastic; no energy is deposited. Compton scatter deposits a small, angularly dependent, energy in the detector. The energy deposited is below the discrimination threshold and is not tracked by the program. It will, however, contribute a small low-energy tail to the spectrum. The main interaction in this energy region is through the photoelectric effect which ejects an electron from an atom of the gas. The energy of the interacting x ray is split between the binding energy of the electron and the kinetic energy of the ejected electron; the electron deposits its kinetic energy in the gas. The hole left in the inner shell (mostly either K or L) of the gas atom will decay, mostly through K- or L-shell fluorescence or by emitting an Auger electron. Inter-shell energy-transfers play a minor role in the detector response. The energy of an Auger electron is quickly absorbed by the counter gas. Fluorescent x rays may be captured or may escape from the counter. Only single x-ray interactions (and the subsequent decays) are tracked by the model.

The flow-logic of the x-ray performance model is illustrated in Figure 4. The software is implemented in Mathematica® 3.0 with the front end running on a Macintosh G3 PowerPC and the kernel running on an SGI Indigo[2] workstation. In operation, the program is set up with an appropriate set of parameters and run. A number of intermediate calculations and data plots are output during the run, culminating in a calculation of the time required for a single detector channel to obtain an SNR of 1:1 for the detection standard. Since the total running time for the program is about 80 s, it is not difficult to evaluate the effects of varying any particular parameter.

The x-ray libraries used contain a number of x-ray related data bases and functions which have been accumulated by the Principal Investigator over a number of years and implemented as Mathematica-callable functions. The various x-ray cross-sections are derived from the Lawrence Livermore National Laboratories EPIC x-ray data tables.

To keep the evaluation time down, the spectrum is broken into discrete (0.5 keV) bins. All interaction coefficients and functions are then defined at the bin energies; this avoids repetitive interpolations from the data base. This also presents a complication for the calculation logistics. In general, x rays which scatter incoherently do not lose energy in multiples of 0.5 keV. In

addition, the width of the energy bins changes after the scatter. The step in Figure 4 called *Generate "Pre-scatter" Spectrum* divides the source into unequal, and unequally-spaced, bins so that the x-ray energies will exactly fit into the final bins *after* the Compton scatter.
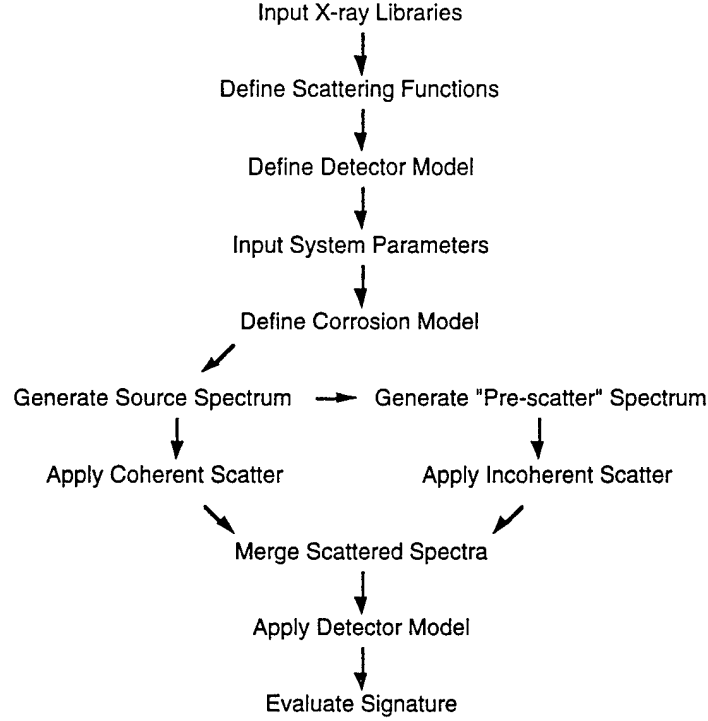
Input X-ray Libraries

Define Scattering Functions

Define Detector Model

Input System Parameters

Define Corrosion Model

Generate Source Spectrum ⟶ Generate "Pre-scatter" Spectrum

Apply Coherent Scatter   Apply Incoherent Scatter

Merge Scattered Spectra

Apply Detector Model

Evaluate Signature

Figure 4. *The calculational flow of the detector-physics model*

The four scattering components (coherent and incoherent from aluminum and oxygen) are computed separately and then merged into a final "scattered" spectrum. Its interaction with the detector physics is then evaluated. At each point in the sample a "coherent" signal S_c and an "incoherent" signal S_i are measured. If we define these signals (counts-per-second) for uncorroded aluminum (S_{Al-I}, S_{Al-I}) and for the oxidized aluminum (S_{AlO-I}, S_{AlO-I}) then we can measure the so-called Rayleigh/Compton (or RC) ratio for the two samples.

$$RC_{Al} = S_{Al-c}\big/S_{Al-i} \tag{3}$$

$$RC_{AlO} = S_{AlO-c}\big/S_{AlO-i} \tag{4}$$

The instrument operates by scanning a region of a lap-joint; the data are presented as an image of the RC ratio. The presence of corrosion is manifested by a pattern of dark splotches on the image

of the lap-joint region. The signature of corrosion can thus be expressed as a ratio of the signals in the corroded and uncorroded regions.

$$Sig = RC_{AlO} \Big/ RC_{Al} \tag{5}$$

Because the contrast of an inspection image on a monitor can be arbitrarily enhanced, the limiting factor in the sensitivity is set by the ratio between the signature and the image noise which is determined by the Poisson statistics of the signals. For a sample time t_s, the standard deviation of the RC ratio (for a single detector) can be found from:

$$\sigma_{RC} = \frac{1}{t_s} \sqrt{\frac{1}{S^2_{Al-c}} + \frac{1}{S^2_{Al-i}}} \tag{6}$$

As discussed above, when the SNR becomes 1:1 (Sig=σ_{RC}), the presence of corrosion becomes evident in the image. For two detectors, and for the final system configuration, the sample time to detect 5% corrosion is found to be:

$$t_s = \frac{1}{2\sigma_{RC}} \sqrt{\frac{1}{S^2_{Al-c}} + \frac{1}{S^2_{Al-i}}} = 0.28s \tag{7}$$

This suggests that a system designed according to this model could scan at 25 m/hr (sampling on a 2-mm grid) and detect 5% corrosion. In comparison with the existing 2-detector breadboard, the sample time is only about 20% shorter. However, because of its integrated detector design, the detector simultaneously measures 40 points across an 80-mm lap-joint, effecting a speedup factor of 50! This completely meets our design goals.

The performance goals for the system have been met by significantly opening up the collimation on the system. In particular, the distance between the drift cathode and the MGC electrode structure is 3–4 times larger than existing detector designs (see Figure 3). In our original proposal we were concerned with the effects of x rays directly impinging on the drift cathode and MGC electrodes. We largely eliminated this problem by bringing in the x rays parallel to the electrodes, so that the direct irradiation was avoided. In the next sections, we will look at the implications of these decisions.

THE ELECTRON CLOUD

As the x rays are absorbed in the counter gas they generate fast electrons which ionize more gas molecules as they scatter and slow down. To measure the energy of the interacting x ray it is

necessary to collect the complete cloud of electrons, thus we need to know how big it is. The RC signature is determined largely by the incoherent scatter peak near 30 keV; this generates photoelectrons in the gas principally in the 15-25 keV range. To determine the size of the generated cloud, a monte-carlo simulation of the electron trajectories was used to define the initial size of the charge cloud created by the photoelectrons. This program, NIST Micro MC, was developed as a software tool for the calculation of the characteristic x-ray emission under electron bombardment and is used to model problems in electron probe x-ray microanalysis and analytical electron microscopy.[15] An image of a simulation of 500 electrons interacting with the gas is shown in Figure 5. In this figure, the electrons enter at the red mark (top center). We can see that few electrons, and very little energy, is deposited more than about 0.75 mm from the point of generation of the photoelectrons.

Eo[kV]=25; Specimen=Xe; Tilt[deg]=0; Traj.No.=500

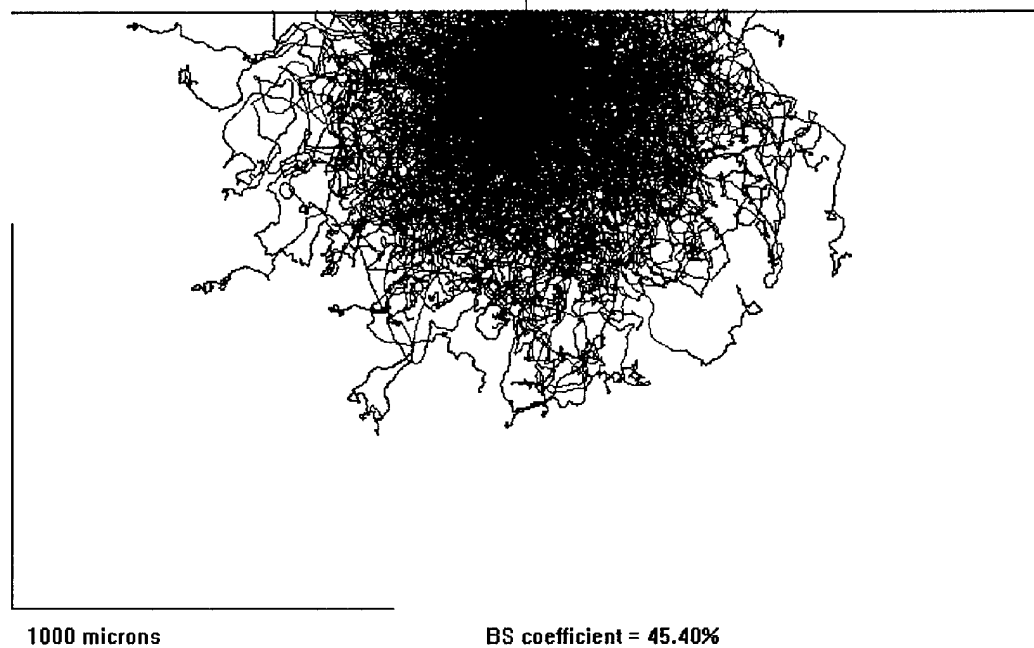1000 microns   BS coefficient = 45.40%

Figure 5.   *A simulation of 25 keV electrons entering the counter gas (2.5 bar) and scattering. As the electron loses energy the color shifts from red to black.*

As each electron track is accelerated to the MGC electrode structure it will continue to diffuse. To evaluate the magnitude of the diffusion, we used results from the Magboltz program which is available from the CERN web-site at http://consult.cern.ch/writeup/garfield. This program does Monte Carlo simulations of charge drift and diffusion for complex mixtures of counter gases in support of gas-counter design for the high-energy physics community. From this software we

were able to obtain diffusion coefficients for drift parallel to [D_p= 0.52 (cm/Bar)$^{1/2}$] and transverse to [D_t= 0.42 (cm/Bar)$^{1/2}$] the electric field for a mixture of 90% Xe/10% CO_2. Broadening of the distribution can be found from:

$$FWHM_p = 2.35\sigma_p = 2.35D_p\sqrt{Z_{drift}/P_{counter}} = 0.53mm \tag{8}$$

$$FWHM_t = 2.35\sigma_t = 2.35D_t\sqrt{Z_{drift}/P_{counter}} = 0.43mm \tag{9}$$

To estimate the effect of diffusion on the breadth of the charge track, these diffusion widths can be convolved with the widths of the charge tracks; this will lead to only a slight broadening of the distribution. In general, we find that the charge tracks will be up to about 0.9-mm in both directions. This has implications for the temporal response of the system and for the charge-collection geometry. The temporal response is limited by the time it takes to collect the full charge cloud. From the Magboltz program were also able to obtain the drift velocity (v_{drift}=0.45 cm/μs) for electrons in the 0.30 V/cm-torr electric field. The collection time t_{coll} is then:

$$t_{coll} = W_{charge}/v_{drift} = 0.2\mu s \tag{10}$$

The peaking time of the pulse amplifier should be no shorter than the collection time.

In order to correctly measure the energy of the x ray, it is necessary to collect all of the electrons resulting from the x ray's electron cloud. Our strategy for making this measurement is illustrated in Figure 6. Groups of MGC anodes are connected together so that they collect the proportional-counter-amplified signals over a 1-mm wide strip. After these signals are amplified and shaped by a fast charge preamplifier/pulse-amplifier combination, they are summed with each adjacent strip. If a given adjacent-strip sum is greater than its neighbors and fits within one of the two discriminator bands used to select either the coherent or incoherent signal, a count is registered in the appropriate register.

The problem addressed by the data-readout strategy is that of partially-collected charge clouds. X rays in the critical 25–30 keV range will, in general, deposit their signal in two adjacent strips. We know from the charge-diffusion studies that it will be very rare for these charges to be distributed into more than two strips. Thus, the comparison of adjacent strip sums will select the pair which captured the full charge. It will then be classified appropriately.
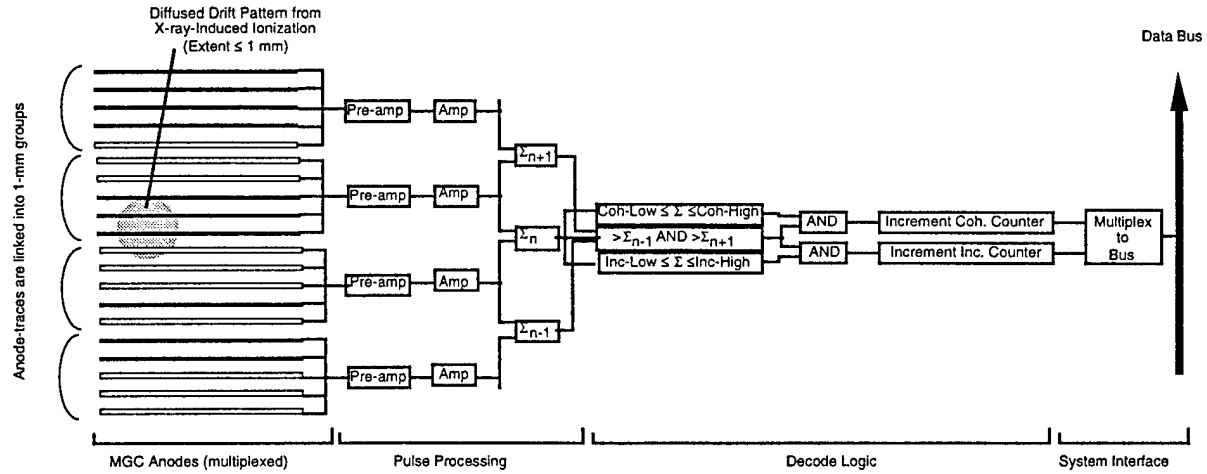
11

Figure 6. *The data readout logic is designed to collect the signal from a diffused charge cloud and determine whether it fits within one of the defined scatter categories.*

The charge-collection strategy will impact the energy resolution of the instrument. Based on the Magboltz results, we can expect the performance of this component of the energy-resolution to be very good below about 30 keV. At higher energies, the charge clouds become larger and, for some interactions, a small part of the signal will not be collected. This loss of resolution at higher energies will not significantly affect the instrument performance as the higher energy x rays are not used in the imaging.

The energy resolution is also affected by the properties of the counter gas. It has been found that the MGC structures have about 20% better energy resolution than standard proportional counters and multi-wire proportional counters (MWPCs).[1] The small increase in counter-gas pressure from 2 to 2.5 Bar (that is in comparison with the breadboard instrument) will tend to offset this improvement as shown in pressure vs. resolution evaluations done for hole-structures.[10] For our application, good energy resolution is useful in maintaining image contrast, but not critical.

ELECTRONICS CONSIDERATIONS

The grouping of the anodes increases the input capacitance of the detector to about 100 pF[1] and presents a potential issue for the ability of the electronics to read out the signal with an acceptable noise level. To verify that our readout-noise goals were reasonable we used a published model for the noise-performance of particle-detector electronics.[16] As inputs to the model, we used the following parameters:

Peaking time (Semi-Gaussian shaping): 0.2 μs,
Total input capacitance: 150 pF,

12

FET transconductance: 17 mS,

Total leakage current: 10 pA,

Total parallel resistance: 100 MΩ,

Temperature: 300 K.

For this type of detector, and at a relatively fast peaking time, the performance is essentially driven by the input capacitance and the transconductance of the FET. For this model, we estimated a readout noise of 1665 electrons. Assuming a targeted avalanche gain of 1000, this noise level is equivalent to approximately 36 eV referred to the x-ray energy. This is negligible in comparison to the ~1000 eV resolution required.

PHOTOEMISSION EFFECTS

The original concept for the detector had the x rays entering through the drift cathode and exiting through the MGC electrode structure. The consequences of photoemission from either electrode surface were of some concern. In the revised concept, the x rays enter through the silicon resistive field plates. We modeled the photoemission from the entrance surface to evaluate the contributions to the detector spectrum. The models extrapolated primary ($\geq$ 50 eV) and secondary ($\leq$ 50 eV) photoemission data which had been taken for x-ray energies from 2.6 to 5.4 keV.[17] Lower-energy data were not used because their primary interaction was with Si-L shell which would not support extrapolation to higher energies.

Extrapolation of the primary photoemission followed the form,[18]

$$Y_p \propto f_p(Ex)\mu_{abs}(Ex)$$ (11)

where the function $f_p(Ex)$ is a slowly varying function of the x-ray energy which approximately follows the energy-dependent range of the most energetic photoelectrons produced by the x rays. The function was empirically fit to the form

$$f_p(Ex) = A + B*Ex + C*Ex^2$$ (12)

The bulk of the primary photoemission is emitted after scattering several times within the solid, leading to a fairly uniform distribution of energies below the "no-loss" escape peak.

Extrapolation of the secondary photoemission followed the form,[18]

$$Y_s \propto f_s(Ex)\mu_{abs}(Ex)Ex$$ (13)

13

where the function $f_s(Ex)$ is a very slowly varying function of the x-ray energy which is more strongly weighted toward the lower-energy photoelectrons produced by the x rays. The function was empirically fit to the form:

$$f(Ex) = D * Ex^{\frac{1}{4}} \tag{14}$$

The secondary photoemission is emitted as a low-energy peak (~1–2 eV). The results of the photoemission model are shown in Figure 7. While the model is probably only accurate within a factor of a few, the contribution (145 electrons/s) is a factor of 1000 lower than the signal due to x-ray interactions in the detector. The photoemission calculation is included as Appendix 1.
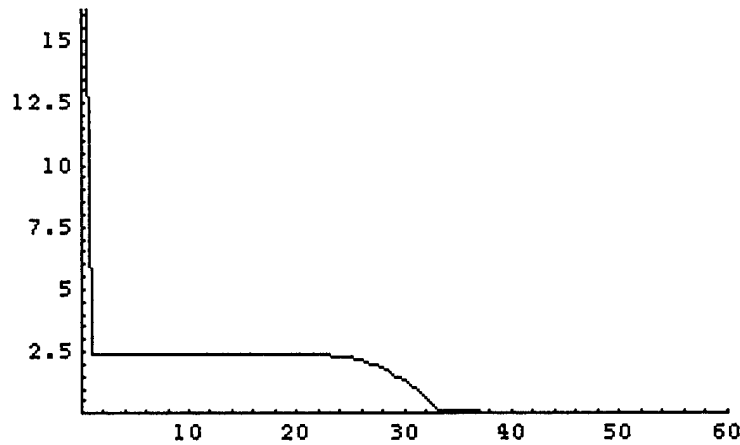

Figure 7. *The modeled photoemission from the silicon field-plate at the entrance to the detector is shown. The vertical axis is electrons/bin, the horizontal axis is the electron energy in keV. Contributions to the overall detector spectrum are completely negligible.*

CONTRIBUTORS

The majority of the technical work and models were done by the Principal Investigator, Dr. Jerel Smith. The monte-carlo calculations of the electron interaction in the gas were provided by Mr. Edward Franco. The evaluations of the electronic noise were contributed by Dr. June Wang.

CONCLUSIONS

This project investigated the use of integrated proportional-counter array technologies to achieve rapid detection of corrosion in aging aircraft lap-joints using ARACOR's COREX inspection technology. The detector technology, developed for use in high-energy physics tracking detectors, promised good spatial resolution and high-speed energy discrimination based on the state of the art. Extending this technique to the detection of corrosion requires that the detectors

operate at higher x-ray energies, with larger inter-electrode spacings, and at reduced spatial resolution. In this project we developed models for the x-ray interactions in the detector and the subsequent electron transport that govern the spatial resolution and temporal response of the detector. This program has been extremely successful, not only in accomplishing the formal goals of developing physics models and evaluating the potential for this technology, but, more importantly, in developing a detector concept that can support nearly two orders-of-magnitude increase in the inspection speed.

This project developed an initial design for a gas micro-strip detector that achieves the performance objectives of the COREX. We demonstrated analytically that this detector, operating at an inter-detector spacing of 2 mm, can achieve count rates above 100,000 Hz. Further, we estimate that the energy resolution of 1 keV is more than adequate for resolving the characteristic signals from coherent and incoherent scatter. The basic conclusion of this project is that this detector technology can provide the basis for a corrosion detection system with a throughput up to 25 m/hr. for the detection of 5% corrosion in lap-joints. Detection of corrosion down to 1% can be accomplished at lower scan speeds.

Following this successful demonstration of feasibility, we recommend that the micro-strip detector be fabricated and experimentally evaluated in a breadboard corrosion-monitor instrument. This will provide direct evidence of the projected sensitivity and system throughput.

REFERENCES

1. F. Angelini, R. Bellazini, A. Brez, G. Decarolis, G. Magazzu, M.M. Massai, G. Spandre, and M.R. Torquati, <u>Nuclear Instruments and Methods in Physics Research</u>, <u>A315</u>, 1992.

2. H.S. Cho, W.S. Hong, N. Palaio, J. Dadyk, K.B. Luk, and V. Perez-Mendez, <u>IEEE Transactions on Nuclear Science</u>, <u>43</u>, 1996.

3. J. Miyamoto and I.P.J. Shipsey, presented at 4th International Conference on Position-Sensitive Detectors, Manchester, September 1996.

4. J. Miyamoto and I.P.J. Shipsey, An Aging Study of Semiconductive Microstrip Gas Chambers and a Gas Electron Multiplier, Dept. of Physics, Purdue University, West Lafayette, Indiana.

5. R. Bouclier, M. Capeans, M. Hoch, G. Million, L. Ropelewski, F. Sauli and T. Temmel-Ropelewski, <u>IEEE Transactions of Nuclear Science</u>, <u>43</u>, 1996.

6. A. Barr, B. Boimska, R. Boucliler, M. Capeans, W. Dominik, G. Manzin, G. Million, M. Hoch, L. Ropelewski, F. Sauli, A. Sharma, presented at 15th International Conference on Advanced Technology and Particle Physics, Como, Italy, October 1996.

7. F. Bartol, M. Bordessoule, G. Chaplier, M. Lemonnier and S. Megtert, <u>J. Phys. III France</u>, <u>6</u>, 1996.

8. F. Sauli, <u>Nuclear Instruments and Methods in Physics Research</u>, <u>A386</u>, 1997.

9. Y. Giomataris, Ph. Rebourgeard, J.P. Robert, G. Charpak, <u>Nuclear Instruments and Methods in Physics Research</u>, <u>A376</u>, 1996.

10. A. Sarvestani, H.J. Besch, M. Junk, W. Meißner, N. Sauer, R. Stiehler, A.H. Walenta, R.H. Menk, <u>Nuclear Instruments in Methods in Physics Research</u>, <u>A410</u>, 1998.

11. A. Sarvestani, H.J. Besch, R.H. Menk, N. Pavel, N. Sauer, C. Strietzel, A.H. Walenta, <u>Nuclear Physics B (Proc. Suppl.)</u>, <u>78</u>, 1999.

12. Ronaldo Bellazini and Mario Alberto Spezziga, submitted for publication in <u>La Rivista del Nuovo Cimento</u>.

13. J. Miyamoto and F.G. Knoll, submitted for publication to <u>Elsevier Preprint</u>.

14. Lawrence B. Levit, Werner D. Farr, Marco L. Vincelli, <u>Nuclear Instruments and Methods in Physcis Research</u>, <u>A235</u>, 1985.

15. Newbury, D. E. and R. L. Myklebust, "NIST Micro MC: A Users Guide to the NIST Microanalysis Monte Carlo Electron Trajectory Simulation Program," <u>Microbeam Analysis</u>, 4 (3) p. 165. 1995.

16. J.S. Iwancyzk, and B.E. Patt, Chapter 14 in <u>Semiconductors for Room Temperature Nuclear Detector Applications</u>, MRS Volume for <u>Semiconductor Semimetals Series</u>, editors: Schlesinger, T.E., and James R.B., 1995).

17. Bernstein, M. J. and J. A. Smith, <u>IEEE Trans. Nucl. Sci.</u> <u>NS-26</u>, No. 6, pp. 1–6, 1979.

18. Henke, B. L. and J. A. Smith, <u>J. Appl. Phys.</u>, <u>48</u>, No 5, pp. 1852–1866, 1977.

■ Appendix 1: AFOSR Detector: Photoemission Evaluation

The objective is to estimate the effect of photoemission from internal detector surfaces on the low-energy end of the spectral response. In this design, the x rays enter from a Be window followed by a 0.1 mm Si sheet, and end in a 0.1 mm Si sheet after passing through 5 cm of 2-atm Xe gas.

```
<< "xSec.m"
```

xSec.m Version 1.1.3, © 1998 Jerel A. Smith

■ Define, Eout, the spectrum into the detector (SpecIn), and the detected spectrum (SpecDet) (taken from "Detector 60 kV, 2.5 bar, 2-mm")

```
L1 = ListPlot[Transpose[{Eout, SpecIn}], PlotRange -> {{0, MaxEi}, {0, Max[SpecIn]}},
    DisplayFunction -> Identity] ;

L2 = ListPlot[Transpose[{Eout, SpecDet}], PlotRange -> {{0, MaxEi}, {0, Max[SpecIn]}},
    PlotJoined -> True, DisplayFunction -> Identity] ;

Show[{L1, L2}, DisplayFunction -> $DisplayFunction] ;
```
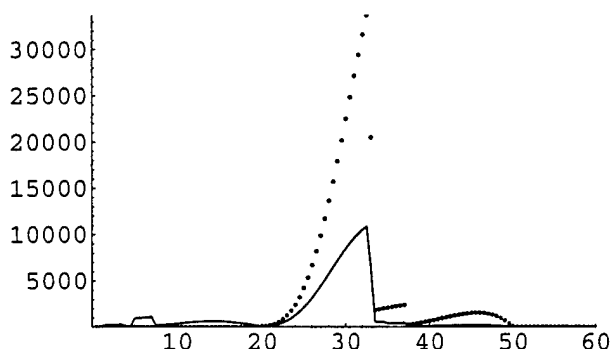

The primary photoemission from the silicon field plate can be estimated from the smith/bernstein measurements. Assume that the primary emission is smeared uniformly from the exciting photon energy to the lowest energy bin. To extrapolate the primary (Yp) and total (Yt) yields , use an empirical power law for the electron ranges:

```
ExTest = {2.64, 4.12, 4.55, 4.95, 5.41} ; (* start above the k-edge*)
YpData = {5.8, 3.5, 3.15, 2.9, 2.63} * 10^-3 ;
YxEMuData = {2.1, 1.85, 1.78, 1.75, 1.82} *10^-6 ; (* divided by Ex Mu (Ex) *)
```

■ Scale the Yp data with the energy-absorption and a power law in Ex

```
YpMu = YpData / muAbs[Si, ExTest]
```

$\{4.09533 \times 10^{-6}, 8.35144 \times 10^{-6}, 9.89986 \times 10^{-6}, 0.0000115531, 0.0000134353\}$

```
Lpd = ListPlot[Transpose[{ExTest, YpMu}], DisplayFunction -> Identity] ;

pRange[x_] = Fit[Transpose[{ExTest, YpMu}], {1, x, x^2}, x]
```
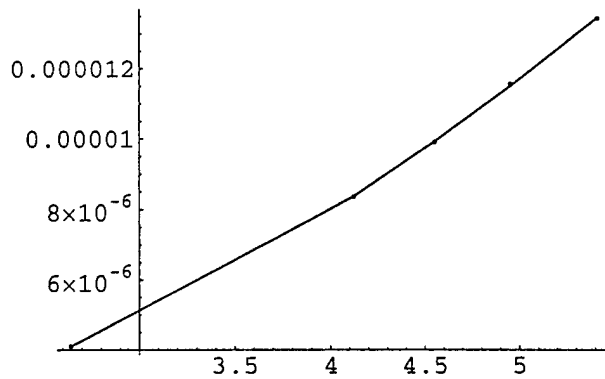
$6.47859 \times 10^{-7} + 2.90772 \times 10^{-7} x + 3.84026 \times 10^{-7} x^2$

```
LpFit = ListPlot[Transpose[{ExTest, pRange[ExTest]}], PlotJoined -> True,
   DisplayFunction -> Identity] ;

Show[{Lpd, LpFit}, DisplayFunction -> $DisplayFunction] ;
```



```
Yp[Ex_] := pRange[Ex] muAbs[Si, Ex] ;
Yp[ExTest] * 10^3   (* check the fit to the original data *)

{5.79529, 3.50546, 3.15678, 2.88586, 2.63496}
```
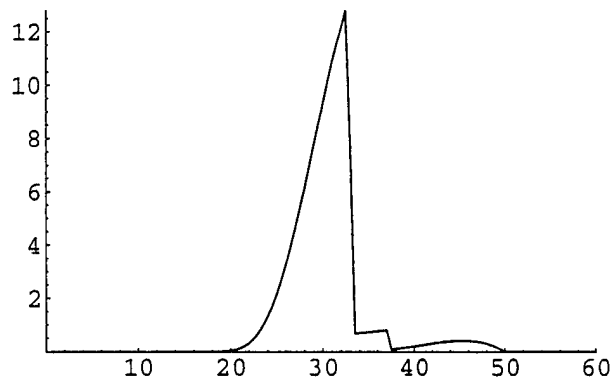
▪ This is the "unsmeared" primary photoemission

```
Sp = Table[SpecIn[[i]] Yp[Eout[[i]]], {i, nPts}] ;

ListPlot[
 Transpose[{Eout, Sp}], PlotRange -> {{0, MaxEi}, {0, Max[Sp]}}, PlotJoined -> True] ;
```



```
Plus@@Sp

144.524
```

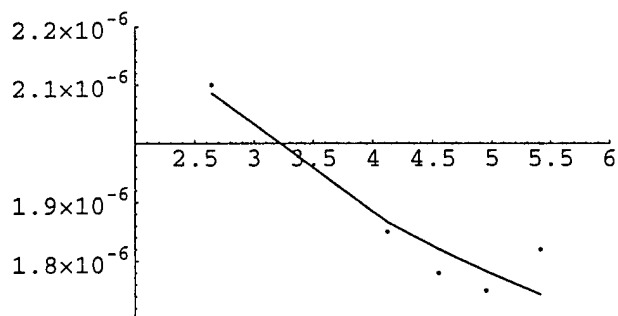## ▪ Let's fit the secondary emission data

```
Lsd = ListPlot[Transpose[{ExTest, YxEMuData}],
   PlotRange -> {{2, 6}, {1.7 * 10^-6, 2.2 * 10^-6}}, DisplayFunction -> Identity] ;
```

```
YsMu[x_] = Fit[Transpose[{ExTest, YxEMuData}], {x^-1/4}, x]
```

$$\frac{2.65899 \times 10^{-6}}{x^{1/4}}$$

```
LsFit = ListPlot[Transpose[{ExTest, YsMu[ExTest]}], PlotJoined -> True,
    PlotRange -> {{2, 6}, {1.7 * 10^-6, 2.2 * 10^-6}}, DisplayFunction -> Identity];
Show[{Lsd, LsFit}, DisplayFunction -> $DisplayFunction];
```



```
Ys[Ex_] := YsMu[Ex] * Ex * muAbs[Si, Ex];
```

```
(Ys[ExTest] + Yp[ExTest]) * 10^3
(* visually check the fit to the original graphed data, ok *)
```

```
{13.5946, 6.72798, 5.79254, 5.10083, 4.48134}
```

```
Ss = SpecIn Ys[Eout];
```

```
Plus @@ Ss
```

```
13.8085
```

■ Now smear the photoemission in energy

■ First the primary photoemission

```
SpecPrim = Table[0, {nPts}];
```
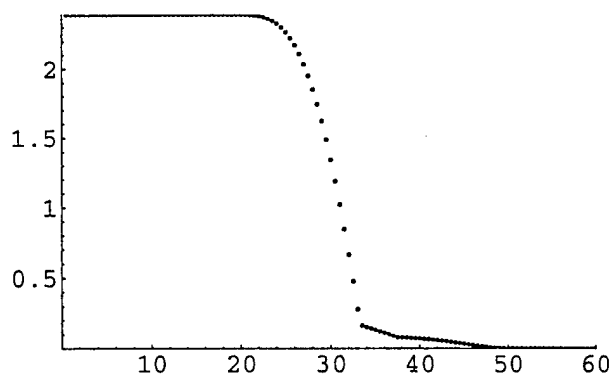
```
For[i = 1, i ≤ nPts, i++,
 newPE = Sp[i] / i;
 For[j = 1, j ≤ i, j++,
   SpecPrim[j] += newPE
   ]]
```

```
ListPlot[Transpose[{Eout, SpecPrim}], PlotRange -> {{0, MaxEi}, {0, Max[SpecPrim]}}] ;
```



```
Plus@@SpecPrim
```

144.524

■ Add the secondary photoemission (all in the bottom bin)

```
SpecTot = SpecPrim ;
SpecTot[[1]] += Plus@@Ss ;

ListPlot[Transpose[{Eout, SpecTot}], PlotRange -> {{0, MaxEi}, {0, Max[SpecTot]}},
 PlotJoined -> True] ;
```